

Rotational orientation effects in NO(X) + Ar inelastic collisions

M. Brouard,^{*,†} H. Chadwick,^{†,§} S.D.S. Gordon,[†] B. Hornung,^{†,||} B. Nichols,[†] F.J.
Aoiz,^{*,‡} and S. Stolte^{*,¶,⊥}

[†]*The Department of Chemistry, University of Oxford, The Physical and Theoretical
Chemistry Laboratory, South Parks Road, Oxford, OX1 3QZ, United Kingdom.*

[‡]*Departamento de Química Física, Facultad de Química, Universidad Complutense, 28040
Madrid, Spain*

[¶]*Institute of Atomic and Molecular Physics, Jilin University, Changchun 130012, China.*

[§]*Current address: Laboratoire de Chimie Physique Moléculaire, Ecole Polytechnique
Fédérale de Lausanne, Lausanne, Switzerland*

^{||}*Current address: School of Chemistry, University of Bristol, Cantock's Close, Bristol,
BS8 1TS, United Kingdom*

[⊥]*Department of Physics and Astronomy, LaserLaB, Vrije Universiteit, Amsterdam, De
Boelelaan 1081, 1081 HV Amsterdam, The Netherlands, and Laboratoire Francis Perrin,
Bâtiment 522, DRECEM/SPAM/CEA Saclay, 91191 Gif sur Yvette, France*

E-mail: mark.brouard@chem.ox.ac.uk; aoiz@quim.ucm.es; stolte@chem.vu.nl

Abstract

Rotational angular momentum orientation effects in the rotationally inelastic collisions of NO(X) with Ar have been investigated, both experimentally and theoretically at a collision energy of 530 cm^{-1} . The collision-induced orientation has been determined experimentally using a hexapole electric field to select the $\epsilon = -1$ Λ -doublet level of the NO(X) $j = 1/2$ initial state. Fully quantum state resolved polarization dependent differential cross sections (PDDCSs) were recorded experimentally using a crossed molecular beam apparatus coupled with a $(1 + 1')$ resonance enhanced multi-photon ionization (REMPI) detection scheme and subsequent velocity-map imaging. In order to determine the NO sense of rotation, the probe radiation was circularly polarized. Experimental orientation polarization dependent differential cross sections are compared with those obtained from quantum mechanical scattering calculations and are found to be in good agreement. The origin of the collision-induced orientation has been investigated by means of close-coupled quantum mechanical, quantum mechanical (QM) hard shell, quasi-classical trajectory (QCT), and classical hard shell calculations at the same collision energy. Although there is evidence for the operation of limiting classical mechanisms, the rotational orientation cannot be accounted for by QCT calculations and is found to be strongly influenced by quantum mechanical effects.

Introduction

After the rotationally inelastic collision of a diatomic molecule with an atom, the molecule can exhibit a preferred sense of rotation, *i.e.* the molecule can preferentially rotate in either a clockwise or a counter-clockwise direction. This preferred sense of rotation corresponds to a positive or negative orientation of the final rotational angular momentum, \mathbf{j}' , with respect to the y -axis of the scattering frame, in which the initial and final relative velocities, \mathbf{k} and \mathbf{k}' lie in the xz plane, with $\mathbf{k} \parallel \mathbf{z}$. The $\mathbf{k}\text{-}\mathbf{k}'\text{-}\mathbf{j}'$ triple vector correlation includes information from both the collision-induced alignment (preferred plane of rotation) and orientation (sense of rotation), and breaks the constraint imposed by the azimuthal symmetry of impact parameters.¹ For the NO(X) + Ar system, the collision-induced alignment has been found to be well-described by a classical kinematic apse model,²⁻⁴ whereas the collision-induced orientation has both classical and quantum mechanical (QM) origins,⁵⁻⁷ and so could provide a more sensitive probe of the collision dynamics. Collision-induced orientation has been investigated theoretically in a number of inelastic⁵⁻⁹ and reactive scattering systems,¹⁰⁻¹³ but there have been very few experimental investigations.^{6,14,15}

NO(X) is a $^2\Pi$ radical with an unpaired electron in a π^* orbital, giving rise to two spin-orbit manifolds, $^2\Pi_{\frac{1}{2}}$ and $^2\Pi_{\frac{3}{2}}$, separated by approximately 123 cm^{-1} . Within each spin-orbit manifold, each rotational level is split into two Λ -doublet sublevels, which are symmetric ($\epsilon = +1, e$) and antisymmetric ($\epsilon = -1, f$) combinations of the $+\Omega$ and $-\Omega$ wavefunctions. For low j states, the Λ -doublet sub-levels are nearly degenerate, but differ in parity, given by $p = \epsilon(-1)^{j-1/2}$. On nonlinear approach of an Ar atom to the NO(X) molecule, the degeneracy of the $^2\Pi$ state is lifted, resulting in two potential energy surfaces of A' and A'' symmetry. In the case of Hund's case (a) molecules, it has been shown^{16,17} that the spin-orbit conserving transitions can be considered to take place on a summed potential

$$V_{\text{sum}}(R, \gamma) = \frac{1}{2}[V_{A'}(R, \gamma) + V_{A''}(R, \gamma)], \quad (1)$$

while spin-orbit changing collisions are coupled by a difference potential

$$V_{\text{diff}}(R, \gamma) = \frac{1}{2}[V_{A''}(R, \gamma) - V_{A'}(R, \gamma)]. \quad (2)$$

Here, $V_{A'}$ and $V_{A''}$ are the potential energy surfaces (PESs) for the two lowest lying electronic states of $\text{NO}(\text{X}) + \text{Ar}$, R is the distance between the Ar atom and the centre of mass of the diatom, and γ is the angle between \mathbf{R} and the NO bond axis, \mathbf{r} .

The $\text{NO}(\text{X}) + \text{Ar}$ system has been the basis of numerous experimental and theoretical investigations. Many of these studies have focused on determining the integral cross sections,^{18,19} as well as lower order vector correlations such as the $\mathbf{k}\text{-}\mathbf{k}'$ correlation, embodied in the differential cross section.^{18,20–31} Parity dependent effects have been observed in both the integral¹⁹ and differential cross sections.^{26–31} More recently, the collision-induced alignment in the $\text{NO}(\text{X}) + \text{Ar}$ system has been investigated experimentally^{4,32} and theoretically,³ and the classical kinematic apse model was found to largely explain the observed rotational alignment. Lorenz *et al.* demonstrated that the rotational orientation of the $\text{NO}(\text{X})$ molecule after collisions with Ar could be determined using circularly polarized light, however, in these experiments the initial Λ -doublet level of the $\text{NO}(\text{X})$ was not selected prior to the collision.⁶ It was found that the experimentally observed orientation oscillated with scattering angle between positive and negative values for low and medium rotational excitation, an effect that was reproduced by quantum mechanical calculations, but not by classical models.⁶ As an antecedent of the present study, the collision-induced alignment and orientation of NO in the $\text{NO}(\text{X}) + \text{Kr}$ system was investigated using the same experimental method as that presented here.¹⁵ However, that study was restricted to the lowest Δj transitions, and did not observe oscillations with scattering angle as only a small angular range was recorded.

In this paper, the collision-induced orientation of the $\text{NO}(\text{X}) + \text{Ar}$ system is investigated experimentally and theoretically. We present here a comprehensive set of fully Λ -doublet state resolved collision-induced orientation data for the first time. We also discuss in detail

the mechanisms responsible for collision-induced orientation, and provide evidence that the observed orientation has a significant quantum mechanical contribution, which cannot be accounted for by classical calculations. Section ‘Methods’ contains details of the experimental methods and theoretical calculations used in the paper. Experimentally determined collision-induced orientation for fully Λ -doublet resolved collisions of $\text{NO(X)} + \text{Ar}$ is presented in Section ‘Experimental results’, where the experimentally determined orientation moments are also compared with corresponding quantum mechanical calculations. In Sections ‘Rotational orientation in classical collisions’ and ‘Quantum mechanical collisions’, the results of the classical and quantum mechanical calculations are compared and discussed. The main findings of the paper are then summarized in Section ‘Conclusions’.

Methods

Experimental methods

The experimental apparatus has been fully described in previous work,^{26,33} and only brief details will be presented here. The fully quantum state resolved polarization dependent differential cross sections (PDDCSs) were recorded experimentally using a crossed molecular beam apparatus coupled with a $(1+1')$ resonance enhanced multi-photon ionization (REMPI) detection scheme and subsequent velocity-map³⁴ imaging.³⁵ The NO molecular beam was generated using a pulse General valve operating at 10 Hz with a backing pressure of 3 bar. The NO was seeded at 16 % in argon to aid adiabatic cooling. The molecular beam then passed through 2 skimmers and entered the hexapole electric field, which exploited the Stark effect to select the $|j = 0.5, \Omega = 0.5, \epsilon = -1\rangle$ quantum state and focused it into the interaction region. The NO molecular beam was then intersected perpendicularly by a beam of Ar atoms. The Ar beam consisted of pure argon and was produced by a General valve operating at 5 Hz to allow shot-to-shot subtraction of any unscattered NO signal.

To allow state selective detection of the scattered NO products, a $(1+1')$ REMPI detection

scheme was employed. 90 % of the 308 nm output of a XeCl excimer laser was used to pump a tunable dye laser. Coumarin 450 dye in methanol was used to achieve lasing at around 452 nm. This was then frequency-doubled to wavelengths around 226 nm, which could be tuned to the particular $\text{NO}(A \leftarrow X)$ rotational transition of interest. The 226 nm beam was directed through a Rochon polarizer, photo-elastic modulator, and $\lambda/4$ plate to generate alternating right and left circularly polarized light. In order to determine the sense of NO rotation in the plane defined by the molecular beams,¹⁵ the probe laser was directed perpendicularly through this plane, passing through a 4 mm diameter hole in the repeller plate as depicted in Figure 1. The remaining 10 % of the 308 nm laser, used to ionize the excited $\text{NO}(A)$ molecules, intersected the molecular beams at 45° in the plane defined by the molecular beams. Velocity map imaging was then employed to image the NO^+ ions.

In the following, the experimental images are presented as the normalized difference $(I_L - I_R)/(I_L + I_R)$ of the individual DCS images recorded using right circularly polarized light (I_R) and left circularly polarized light (I_L).³⁶ This minimizes flux-density and differential cross section effects on the observed orientation.^{4,32} The experimental images were then fit in Fourier moment space using an iterative fitting method that has been fully described previously.^{4,37}

Polarization dependent differential cross sections

The results presented here are shown in the scattering frame, in which the relative velocity, \mathbf{k} , defines the direction of the z axis. The final relative velocity after the collision, \mathbf{k}' , is taken to lie in the xz plane, with $x > 0$, while the y axis is chosen to have a right handed frame of reference.

The classical probability that a particle is scattered through an angle, θ , with its rotational angular momentum, \mathbf{j}' pointing in a direction $(\theta_{j'}, \phi_{j'})$ is given by¹²

$$P(\cos \theta, \cos \theta_{j'}, \phi_{j'}) = \sum_{kq} \frac{2k+1}{4\pi} \left(\frac{2\pi}{\sigma} \frac{d\sigma_{kq}}{d\omega} \right) C_{kq}^*(\theta_{j'}, \phi_{j'}), \quad (3)$$

where the $C_{kq}^*(\theta_{j'}, \phi_{j'})$ are the complex conjugates of the modified spherical harmonics and the expansion coefficients, $n_q^{(k)}(\theta) \equiv (2\pi/\sigma)d\sigma_{kq}/d\omega$, are the normalized PDDCSs, which are the polarization moments that characterize the distribution of the final rotational angular momentum of the scattered particles as a function of scattering angle.¹²

Quantum mechanically, the un-normalized PDDCSs can be calculated according to³⁸

$$\frac{d\sigma_{kq}}{d\omega} = \frac{1}{2j+1} \sum_{m, m'_1, m'_2} f_{jm\Omega\epsilon \rightarrow j'm'_1\Omega'\epsilon'}(\theta) f_{jm\Omega\epsilon \rightarrow j'm'_2\Omega'\epsilon'}^*(\theta) \langle j'm'_1, kq | j'm'_2 \rangle, \quad (4)$$

where $f_{jm\Omega\epsilon \rightarrow j'm'_1\Omega'\epsilon'}(\theta)$ is the scattering amplitude for the transition with the indicated quantum numbers, σ is the integral cross section for the transition, and $\langle j'm'_1, kq | j'm'_2 \rangle$ is a Clebsch-Gordan coefficient. The normalized PDDCS is given by³⁸

$$n_q^{(k)} = \frac{2\pi}{\sigma} \frac{d\sigma_{kq}}{d\omega} = \frac{2\pi}{\sigma} \frac{1}{2j+1} \sum_{m, m'_1, m'_2} f_{jm\Omega\epsilon \rightarrow j'm'_1\Omega'\epsilon'}(\theta) f_{jm\Omega\epsilon \rightarrow j'm'_2\Omega'\epsilon'}^*(\theta) \langle j'm'_1, kq | j'm'_2 \rangle. \quad (5)$$

The renormalized PDDCSs are then given by³⁸

$$\begin{aligned} \rho_q^{(k)}(\theta) &= \frac{(d\sigma_{kq}/d\omega)}{(d\sigma_{00}/d\omega)} = \frac{n_q^{(k)}}{n_0^{(0)}} = \\ &= \frac{\sum_{m, m'_1, m'_2} f_{jm\Omega\epsilon \rightarrow j'm'_1\Omega'\epsilon'}(\theta) f_{jm\Omega\epsilon \rightarrow j'm'_2\Omega'\epsilon'}^*(\theta) \langle j'm'_1, kq | j'm'_2 \rangle}{\sum_{m, m'} |f_{jm\Omega\epsilon \rightarrow j'm'\Omega'\epsilon'}(\theta)|^2}. \end{aligned} \quad (6)$$

$(d\sigma_{00}/d\omega)$ is the $k=0, q=0$ PDDCS, which is equal to the differential cross section, and quantifies the angular distribution of the scattered products.

Finally, the integral polarization parameters (PP) can be obtained upon integration of the normalized PDDCS over the scattering angle. Thus, specifically for the orientation PP we have:

$$a_{1-}^{\{1\}} = \int_{-1}^{+1} n_{1-}^{\{1\}}(\theta) d\cos\theta. \quad (7)$$

The limits of the PP coincide with those of the renormalized PDDCS and are function of the j' value.

The PDDCSs and PPs are in general complex, and so the real PDDCSs $n_{q\pm}^{\{k\}}(\theta)$ and PP $a_{q\pm}^{\{k\}}$ are obtained using the Hertel-Stoll convention.^{12,39}

As will be seen in the following, it is also convenient to define the classical polarization dependent partial cross section (PDPCS) as

$$\sigma_q^{\{k\}}(b) = 2\pi b P_q^{\{k\}}(b) \quad (8)$$

where $P_q^{\{k\}}(b)$ is a polarization dependent opacity function. For $k = q = 0$

$$\sigma_0^{\{0\}}(b) = 2\pi b P(b), \quad (9)$$

with

$$\int_0^{b_{\max}} \sigma_0^{\{0\}}(b) db = \sigma. \quad (10)$$

Of more interest is the *normalized* polarization dependent partial cross section (n-PDPCS):

$$p_q^{\{k\}}(b) = \frac{2\pi}{\sigma} b P_q^{\{k\}}(b) = \frac{\sigma_q^{\{k\}}(b)}{\sigma}. \quad (11)$$

It is easily shown that the integral polarization parameters, $a_q^{\{k\}}$, are related to the n-PDPCS *via*:

$$a_q^{\{k\}} = \frac{2\pi}{\sigma} \int_0^{b_{\max}} b P_q^{\{k\}}(b) db = \int_0^{b_{\max}} p_q^{\{k\}}(b) db \quad (12)$$

Classical hard shell calculations

Spin-orbit conserving transitions take place on the $V_{\text{sum}}(R, \gamma)$ potential energy surface in the Hund's case (a) limit.^{16,40} Therefore, the quasi-classical trajectory (QCT) and classical hard shell calculations were carried out on the $V_{\text{sum}}(R, \gamma)$ potential energy surface. Except

for an attractive well of approximately -110 cm^{-1} depth at larger inter-particle separations, the potential is strongly repulsive. It is thus reasonable to model the $V_{\text{sum}}(R, \gamma)$ potential with a hard shell potential, *i.e.* a potential which is infinite inside a contour and zero outside of that at the present collision (here also total) energy of 530 cm^{-1} .^{7,41} The comparison of the results obtained on this hard shell PES with calculations employing the full or modified ‘soft’ repulsive PESs⁴¹ (see Section ‘QCT calculations’) helps to identify the role of different parts of the potential in determining the collision-induced rotational orientation. The two-dimensional (2D) hard shell contour, with $C_{\infty v}$ symmetry, was obtained as the intersection between the $V_{\text{sum}}(R, \gamma)$ potential and the collision energy.⁷ The method of Beck and Ross was adopted in order to carry out the hard shell calculations.^{42–45} The details of the Monte Carlo calculations were described in Ref. 7. A single batch of 7×10^6 inelastic trajectories was analyzed to obtain the PDDCSs and partial cross sections presented in Section ‘Results and Discussion’.

QCT calculations

The details of the QCT calculations employed in this work are described elsewhere^{7,25,46} and only those aspects that are specific to this work are described here. The trajectory calculations employed the $V_{\text{sum}}(R, \gamma)$ of Alexander.¹⁹ The classical equations of motions were solved while the N–O interatomic distance was kept fixed using the method of Lagrange multipliers. The square of the classical angular momentum was equated to $j'(j' + 1)\hbar^2$, and the values of j' were then rounded to the nearest integer. The maximum value of the impact parameter was determined as 6.3 \AA , beyond which no trajectories lead to inelastic collisions.

In order to ascertain the effects of the finite range repulsion in the absence of the attractive features of the potential, a ‘soft’ potential was constructed. This ‘soft’ potential is purely repulsive, the attractive parts having been removed using an appropriated damping function:⁴¹

$$f(R, R_0, R_{\text{shift}}, \alpha) = 1 - \frac{1}{1 + \exp(-\alpha(R - R_0 + R_{\text{shift}}))}, \quad (13)$$

where α , R_0 , $R_{\text{shift}} > 0$, and α determines the steepness of the function. R_{shift} shifts the inflexion point of $f(R, R_0, R_{\text{shift}}, \alpha)$ towards smaller R , so that scaled potentials drops below a pre-defined small value of $\varepsilon \times E_{\text{coll}}$ at a distance of R_0 . ε was chosen to be 10^{-2} . R_0 is the contour of the $V_{\text{sum}}(R, \gamma)$ PES at zero collision energy. As such it depends on γ , the Jacobi angle. A comparison of the soft and full potentials can be found in Ref. 41.

The sum and difference PESs can then be written as:

$$\tilde{V}_{\text{sum}}(R, \gamma_i) = V_{\text{sum}}(R, \gamma_i) f(R_i, R_{0,i}, R_{\text{shift},i}, \alpha_i) \quad (14)$$

$$\tilde{V}_{\text{diff}}(R, \gamma_i) = V_{\text{diff}}(R, \gamma_i) f(R_i, R_{0,i}, R_{\text{shift},i}, \alpha_i), \quad (15)$$

where the index, i , runs over the Jacobi angles at which the original A' and A'' PESs were calculated.¹⁹ In this manner it is possible to modify both $V_{\text{sum}}(R, \gamma)$ and $V_{\text{diff}}(R, \gamma)$ so that they remain the half sum and half difference of the $V_{A'}$ and $V_{A''}$ potentials. In the present calculations, α_i was set in the range 1.0 bohr^{-1} to 5.0 bohr^{-1} , and $R_{\text{shift},i}$ in the range 1.0 bohr and 0.50 bohr . The scattering results are quite similar within these ranges of parameters.

QM hard shell calculations

The method of Bosanac and Petrović^{47,48} was used to solve the quantum mechanical scattering problem of a point-like atom and a hard shell.⁷ The 2D hard shell contour was identical to that used in the classical hard shell calculations. Rotational states up to $j = 23$ and partial waves up to $J = 100$ were included in the scattering wavefunction in order to achieve convergence.⁷

QM close-coupled calculations

Full non-adiabatic close-coupled calculations were carried out on the $V_{\text{sum}}(R, \gamma)$ and $V_{\text{diff}}(R, \gamma)$ coupled-cluster singles, doubles, perturbative triples (CCSD(T)) PESs of Alexander¹⁹ using the Hibridon suite of codes.⁴⁹ The PESs were calculated with the N–O bond length kept fixed

at its equilibrium value.¹⁹ As a consequence, the vibrational degree of freedom is ignored in the calculations presented in this paper. The collision energy was set to 530 cm^{-1} ($\approx 66\text{ meV}$), which corresponds to the mean experimental collision energy. Rotational levels up to $j' = 20.5$, both Λ -doublet levels ($\epsilon = -1, +1$) and spin-orbit manifolds ($\Omega = 0.5, 1.5$) were included in the scattering wavefunction. The maximum partial wave was set to $J = 160.5$ in order to achieve convergence which corresponds to a classical impact parameter of 6.8 \AA . In the case of ‘soft’ potential calculations, both $V_{\text{sum}}(R, \gamma)$ and $V_{\text{diff}}(R, \gamma)$ were scaled according to Eqs. (13)–(14). In addition to the open shell calculations, closed shell scattering calculations were carried out on the V_{sum} PES, in which the NO(X) were treated as a closed shell molecule in order to provide a direct comparison to QCT and QM hard shell results.

Results and Discussion

Experimental results

Images and experimental PDDCSs

Figure 2 shows the experimental difference ($I_L - I_R$), normalized difference $(I_L - I_R)/(I_L + I_R)$, along with the individual DCS images recorded using right and left handed circularly polarized light (RCP and LCP) for a range of spin-orbit conserving $f - f$ transitions. The NO is probed using $R_{21}\uparrow$ branch excitation, and so RCP preferentially detects molecules rotating in an anti-clockwise direction in the plane of the molecular beams, such that \mathbf{j}' is directed anti-parallel to the laser propagation axis. Molecules rotating in a clockwise direction are preferentially detected with LCP. Therefore, negative intensity indicates an anti-clockwise rotation in the plane defined by the molecular beams and positive intensity corresponds to clockwise rotation.^{6,36}

The difference and normalized difference images show a sign inversion when reflected in the perpendicular plane containing the relative velocity (indicated by a white arrow). This

can be understood by considering the direction of the scattering frame y -axis for different parts of the image. Figure 3 illustrates the angular momentum orientation after a collision for $\Delta j = 12.5$. Trajectories that result in scattering to the slow side of the image (to the bottom left of the relative velocity) rotate in a clockwise direction and show positive intensity. Since the orientation is defined relative to the scattering frame y -axis, this corresponds to negative orientation (*i.e.* \mathbf{j}' is oriented anti-parallel to the scattering frame y -axis). Trajectories that scatter through the same angle, θ , into the fast side of the image (top right of the relative velocity) rotate in an anti-clockwise direction in the laboratory and so are preferentially detected by RCP light and are shown by negative intensity. Although these molecules have the opposite sense of rotation in the plane defined by the molecular beams, the scattering frame has been inverted due to the change in direction of \mathbf{k}' , and so the orientation in the scattering frame is still negative.

In areas of the experimental DCS images where the signal intensity is low, such as the center of the image, it is not possible to gain orientation information. In some DCS images (for example, for $j' = 11.5$), experimental background can be seen in the backwards scattered direction (see Figure 2). Since the excitation laser was passed through a small hole in the charged repeller plate, it is possible that slight clipping of the plate by the beam could result in ejection of electrons from the charged plate. These electrons may have been able to ionize Ar from the secondary beam and so caused increased experimental background signal in the backwards scattered direction.

Figure 4 displays the experimental and fitted normalized difference images. Agreement between the fitted and experimental images is good, lending confidence that a sufficient number of moments has been applied in the fitting process to reproduce the experimental data. A threshold was applied to the experimental and fitted images, such that where the experimental intensity, or QM DCSs are small, the normalized difference image is set to zero. Experimentally determined $\rho_{1-}^{\{1\}}(\theta)$ orientation moments are shown in the middle column of Figure 5, along with those obtained from QM calculations. The agreement between the

experimental and theoretical $\rho_{1-}^{\{1\}}(\theta)$ PDDCSs is rather good. The main disagreements are due to lack of experimental intensity in the image, for example in the forwards scattered direction $j' = 12.5, f$. The magnitude of the positive orientation in the experimental fits is also slightly less than the QM calculation for sideways scattering in $j' = 7.5$ and $j' = 9.5$ ($\Delta j = 7$ and 9 , respectively). In the case of the collision-induced rotational alignment of NO by Kr,³⁷ it was proposed that secondary inelastic collisions were responsible for a slight reduction in collision-induced alignment moments compared with theory. This does not appear to be the issue with the present orientation measurements, since depolarizing collisions would be likely to affect both positive and negative orientation. In contrast to the alignment measurements in NO + Kr, in the case of NO + Ar, the negative orientation is not significantly underestimated. This seems to rule out secondary collisions as a potential explanation for the discrepancy between theory and experiment for $j' = 7.5$ and $j' = 9.5$.

A positive value of $\rho_{1-}^{\{1\}}(\theta)$ indicates that the rotational angular momentum \mathbf{j}' lies preferentially parallel to the scattering frame along the $+y$ semi-axis, while a negative value corresponds to \mathbf{j}' along to $-y$. For the lowest j' transition recorded, the experimental and QM $\rho_{1-}^{\{1\}}(\theta)$ PDDCSs oscillate between positive and negative values over the entire angular region. As j' increases, the frequency of these oscillations can be seen to decrease, and $\rho_{1-}^{\{1\}}(\theta)$ becomes negative over a larger angular range. As will be discussed in the following sections, the orientation becomes increasingly negative due to the more repulsive nature of the collisions. The decrease in frequency of the oscillations observed in the experimental and QM PDDCSs has been rationalized in terms of the outgoing de Broglie wavelength for the system.⁷ As the rotational excitation of the NO increases, the final relative velocity of the system decreases, resulting in a corresponding increase in the outgoing de Broglie wavelength. The observed oscillatory behavior of the $\rho_{1-}^{\{1\}}(\theta)$ PDDCS is in agreement with previous measurements of collision-induced orientation in the NO(X) + Ar system by Lorenz *et al.*,⁶ although the exact details of the oscillations differ due the initial Λ -doublet selection in the current work.

Experimental and QM normalized angular distributions, $P(\theta)$ (that is, the normalized DCSs, $n_0^{(0)}(\theta)$), are also shown in the first column of Figure 5. The experimental normalized (11-) orientation PDDCSs, $n_{1-}^{\{1\}}(\theta)$, are calculated multiplying the renormalized $\rho_{1-}^{\{1\}}(\theta)$ PDDCSs by the normalized angular distributions. The third column of Figure 5 displays the experimental and QM $n_{1-}^{\{1\}}(\theta)$ PDDCSs. Again, the agreement between experiment and theory is good, reflecting that found for the angular distributions and $\rho_{1-}^{\{1\}}(\theta)$ PDDCSs.

A comparison of QM and QCT simulations is shown in Figure 6, along with the corresponding experimental images. A threshold has been applied to the experimental, QM, and QCT simulated images, such that where the experimental intensity is low or the calculated DCS drops below a specified value, the normalized difference image is set to zero. The QM simulations reproduce the features seen experimentally, including the sign changes in the orientation.

However, it is clear that the QCT simulations are unable to reproduce the collision-induced orientation observed in the experimental images. The dominant feature in the QCT simulations is the intense peak in the orientation predicted in the forwards scattered direction, which increases in intensity and becomes broader as the rotational excitation increases. The peak in the orientation is seen clearly in the QCT renormalized $\rho_{1-}^{\{1\}}(\theta)$ PDDCSs (the right most column in Figure 6), which shows negative peaking orientation at scattering angles around $\theta \simeq 0^\circ$ for $\Delta j = 6$ and $\theta \simeq 30^\circ$ for $\Delta j = 12$. The peak in the QCT predicted orientation is also clearly observed as an intense orientation feature in the QCT simulated normalized difference images (third column of Figure 6). To the left of the relative velocity, the intense peak in the QCT predicted normalized difference images is positive, indicating rotation of the NO in a clockwise direction in the lab frame, and therefore negative orientation of \mathbf{j}' with respect to the scattering frame y -axis, as shown in Figure 3. This propensity for negative orientation in the forwards scattered direction is also seen in the experimental and QM images for $j' \geq 8.5$, however, it is much less pronounced than in the QCT simulations, as is evident from comparison of the QM and QCT renormalized

$\rho_{1-}^{\{1\}}(\theta)$ PDDCSs shown in Figure 6. Again, negative orientation can be seen in both sets of calculations at small scattering angles, however, the agreement between the QM and QCT calculations is far from quantitative, with oscillations observed in the QM calculations that are not reproduced by the classical calculations.

Experimental integral orientation moments

Experimentally determined, QM, and QCT calculated $a_{1-}^{\{1\}}$ integral orientation moments, that are obtained by integrating the corresponding normalized PDDCSs, eq. 7, are compared in Figure 7. The experimental and quantum mechanical moments are in good agreement, although some discrepancies for $\Delta j = 7$ and $\Delta j = 9$ can be seen, perhaps due to the disagreement in the $\rho_{1-}^{\{1\}}(\theta)$ in the region of the sharp feature at sideways scattered angles (around 90°), as seen in Figure 5. Both the experimental and QM data show the parity dependent alternations with rotational state, which are not observed in the QCT calculations. All three sets of data show the same general trend, with the orientation moment becoming more negative with increasing Δj as a consequence of the increasing repulsive nature of the collisions. The good agreement between the general trend of the QCT and experimental and QM data confirm that the limiting attractive and repulsive classical mechanisms, that will be discussed in the following sections, also play a role in the quantum mechanical scattering of NO(X) by Ar.

Rotational orientation in classical collisions

Classical hard shell calculations

The simplest model in which to consider collision-induced orientation is that of a classical hard shell collision. It has previously been found that there cannot be net rotational orientation in *classical* single-encounter collisions of a hard shell and an structureless atom.⁴⁵ These encounters take place at an infinitely small point on the molecular surface in an infinitely short interaction time. Under these circumstances, the body fixed frame components of the

final rotational angular momentum, \mathbf{j}' , are determined by the point-of-contact, the surface normal at this point, and by the projection of the initial relative linear momentum onto the surface normal (see Figure 8).⁴² Therefore, there is cylindrical symmetry of the trajectories about the surface normal, which leads to identical \mathbf{j}' in the body fixed frame. However, the scattering frame will be different for each of these collisions in the body fixed frame, since the scattering frame is defined by the initial and final relative velocities. Those collisions which are related by a rotation through an angle of π about the surface normal are associated with scattering frames whose y -axis are anti-parallel. Therefore, the two rotational orientations will be equal with respect to their modulus, but have different signs. Thus, although each individual collision results in a specific sense of rotation of the molecule, for every impact that results in a clockwise rotation, an equivalent encounter at the same point on the molecule, leading to the same scattering angle and Δj , will induce equal and opposite anti-clockwise rotation, and hence no net orientation can take place. It is worth noting that one of the equivalent trajectories is usually associated with small impact parameters and shallow incident Jacobi angles with respect to molecular bond axis, while the other is characterized by larger impact parameters and Jacobi angles closer to 90° , as shown in Figure 8. As discussed further below, the symmetry of such encounters may be removed by secondary hard shell collisions with the diatom,^{2,45} giving rise to net rotational orientation.

Figure 9 displays the $\rho_{1-}^{\{1\}}(\theta)$ renormalized PDDCSs, and the $n_{1-}^{\{1\}}(\theta)$ normalized PDDCSs, obtained from classical hard shell calculations for a selection of final states, resolved into those which result in positive (+) and negative (−) orientation. Here, the symmetry between collisions resulting in positive and negative orientation can clearly be seen. The total normalized orientation PDDCSs, $n_{1-}^{\{1\}}(\theta)$, is the sum of the two orientation resolved PDDCSs, and hence it vanishes for all scattering angles and final states, resulting in no net orientation. The double peaked structure in the $n_{1-}^{\{1\}}(\theta)$ PDDCS reflects the angular distribution of the scattered products.

Orientation resolved normalized polarization dependent partial cross sections, n-PDPCSs,

are also shown in the bottom row of Figure 9, in which the final rotational orientation is plotted as a function of the initial impact parameter, b . The n-PDPCSs are obtained using eq. 12. As shown in the figure, the positive and negative contributions to the total n-PDPCS do not cancel out at each impact parameter, however, when integrated over all impact parameters, the net orientation is zero. It is clear from the n-PDPCSs, that high impact parameter collisions result in negative orientation, whereas positive orientation results from collisions at smaller impact parameters.

Classical full and soft potential calculations

As discussed above, in the case of classical hard shell collisions, the number of trajectories leading to positive orientation is equal to that leading to negative orientation. However, when considering the full potential, attractive and soft repulsive parts of the interaction potential perturb the classical hard shell trajectories, and the balance between the positive and negative orienting trajectories is disrupted, resulting in non-vanishing rotational orientation. As a consequence, in general there will be collision-induced rotational orientation if a finite range potential acts on the classical system.⁷

If the interaction is governed by the full potential, as shown in the top panels of Figure 10, the symmetry of the $(-)$ and $(+)$ orientation resolved normalized PDDCSs, $n_{1-}^{\{1\}}(\theta)$, is broken for almost all scattering angles and final states. For low Δj transitions, a positive peak is observed at small scattering angles, as shown in the left panel of Figure 10. This is due to the long range attractive forces, which result in an anti-clockwise sense of rotation. This is confirmed by the orientation resolved n-PDPCSs, where the main positive contribution to the orientation is found at impact parameters between 3.5 \AA and 5.5 \AA , for which trajectories mostly sample the attractive well. The mechanism responsible for the positive orientation, *i.e.* \mathbf{j}' along $+y$, can be summarized as follows: for large enough impact parameters, the collisions takes place on the attractive part of the potential. As the atom passes by the diatom it is deflected to the far-side of the molecule. The diatom rotates in the direction of

the departing atom, due to the attractive nature of the interaction. Therefore, the rotational orientation will be positive in the scattering frame. The attractive well is less capable of inducing transitions to higher j' states, thus this mechanism gradually becomes less prominent and disappears for $\Delta j \gtrsim 3$. For transitions in the range $\Delta j \approx 5$ to 7, attractive and repulsive forces nearly balance each other, leading to small net rotational orientation, as shown in the middle panel of Figure 10.⁷

Naively, one might expect that the orientation vanishes as the collision becomes more impulsive, or hard shell like, with increasing Δj , however, this is clearly not the case. The overall rotational orientation gradually becomes more negative, *i.e.* \mathbf{j}' along $-y$, for high Δj transitions as a consequence of the lessening weight of the $(+)$ $n_{1-}^{\{1\}}(\theta)$ orientation resolved PDDCS with respect to its negative counterpart, shown the rightmost columns of Figure 10.

The roles of the attractive and repulsive forces can be further explored by comparing calculations performed using the full and soft repulsive potentials. The purely repulsive soft potential was constructed using eqs. 13–14. The $(+)$ and $(-)$ orientation resolved PDDCSs almost perfectly cancel each other for low Δj transitions, recovering the classical hard shell case, as shown in the left panels of Figure 11. For high Δj transitions, the total and orientation-resolved PDDCSs and n-PDPCSs are similar to those obtained employing the full potential, as can be concluded from the comparison of the right panels of Figures 10 and 11. There is a clear propensity for collisions that result in high rotational excitation to lead to negative, or clockwise, final rotational orientation. This implies that in the case of real collisions on the full potential, repulsive forces are responsible for the rotational orientation in the case of high rotational excitation. However, note that the repulsive interaction must operate over a finite range for the collision-induced orientation to be observed in classical calculations.

Two limiting classical mechanisms causing collision-induced rotational orientation have thus been identified.⁷ For low Δj transitions, long range attractive forces deflect the atom to the far side resulting in positive rotational orientation. For high Δj transitions, the short

range repulsive forces repel those atoms that approach the diatom at shallow Jacobi angles, and would otherwise lead to positive rotational orientation. As a consequence, the rotational orientation is negative.

As a final remark, the definition and the possible role of the chattering collisions^{8,45} should be clarified. In the case of hard shell scattering, a collision is called chattering if the atom suffers an encounter with the diatom multiple times. We did not find any evidence for this type of collision using the exact hard shell contour at a collision energy of 530 cm⁻¹ (66 meV). If the interaction potential is smooth, a chattering collision refers to an event where the final rotational angular momentum is lower than the maximum rotational angular momentum achieved during collision.⁸ Since the interaction is continuous, it can be considered as an prolonged interaction, rather than a sequence of two separate collisions. To conclude, we do not believe that chattering collisions are responsible for the pronounced orientation observed on either the full, the soft, or hard shell PESs, under the present collision energy conditions. Indeed, on the contrary, there is evidence that chattering collisions in NO(X) + Ar can lead to a decrease in the orientation and alignment of the final rotational angular momentum.⁸

Quantum mechanical collisions

Closed shell calculations on the soft repulsive and full PESs

Closed shell quantum mechanical calculations were performed on the soft repulsive $V_{\text{sum}}(R, \gamma)$ potentials. Closed shell, close-coupled renormalized $\rho_{1-}^{\{1\}}(\theta)$ PDDCSs calculated using the full and ‘soft’ potentials, as well as those obtained with the QM hard shell approximation are compared in Figure 12 for the indicated Δj transitions. The QM calculated orientation moments on the full, soft, and hard shell PESs all show a number of features in common, which are not present in the classical calculations. All show changes in sign of orientation as a function of scattering angle, although the precise angles at which these sign changes occur varies somewhat with choice of PES. Furthermore, at small scattering angles, the orientation moments display rapid diffraction-type oscillations. These oscillations are more evident for

small Δj transitions. These rapid diffraction-type oscillations are not observed in the present experiments, because the latter are of insufficient angular resolution.

The classical roles of the attractive and repulsive features of the $V_{\text{sum}}(R, \gamma)$ potential can easily be recognized in the QM orientation data. A positive orientation lobe is observed in the forward scattered region for low Δj collisions in the case of the full potential, for which the attractive region of the PES is present. This feature is absent in the ‘soft’ potential and hard shell cases, showing that the attraction is responsible for the positive orientation for these low final rotational states. The three calculations differ mostly for the medium Δj transitions, whereas the results are very similar for high rotational excitation. As a matter of fact, the rotational orientation is virtually completely determined by the hard shell interaction for $\Delta j > 14$.

Quantum mechanical hard shell collisions

The details of the QM hard shell calculations were discussed in Section ‘QM close-coupled calculations’. They provide an important benchmark for the current study. Unlike the classical collisions of hard shell atoms and molecules, which does not give rise to any collision-induced orientation, QM collisions between hard shell species generally do result in rotational orientation.⁷ The orientation observed in the hard shell QM case arises from the non-local nature of the quantum mechanical interactions.⁷ The incoming atom interacts with the diatom over a finite region of the hard shell potential, determined by the de Broglie wavelength of the system. There is no well-defined point of contact, leading to the breakdown of the rotational symmetry about the surface normal that was responsible for the lack of rotational orientation observed in classical hard shell collisions.⁷ Furthermore, the interaction also takes place over a finite lapse of time, during which the diatom rotates. This invalidates one of the classical hard shell requirements for vanishing rotational orientation, namely the interaction should happen in an infinitely short period of time. This point can be demonstrated by artificially reducing the rotational constant of the NO(X) molecule, thereby making it rotate more

slowly. This results in a reduction in the calculated collision-induced rotational orientation, as demonstrated in the top row Figure 13.

Conversely, longer de Broglie wavelengths are expected to be associated with stronger collision-induced rotational orientation, because the interaction becomes less localized on the molecular surface.⁷ This can be demonstrated by carrying out a series of calculations in which the reduced mass of the system is decreased by a factor of 4 and 64, in order to lengthen its de Broglie wavelength by a factor of 2 and 8. The longer the de Broglie wavelength, the more strongly \mathbf{j}' is oriented, as seen in the bottom row of Figure 13.⁷

The QM hard shell mechanism is unique, in the sense that it has no classical counterpart. It arises purely due to the quantum mechanical nature of the interaction.⁷ It is expected that this QM mechanism will play a dominant role in collisions where the interaction potential is steeply repulsive, such as in the collisions of NO(X) with He or Ne.

Integral orientation moments

As observed experimentally, the Λ -doublet resolved QM $a_{1-}^{\{1\}}$ moments, obtained using eq. 7, show a decreasing trend in orientation with increasing Δj , superimposed with parity dependent oscillations (see the left panel of Figure 14). The phase of the oscillations is opposite for transitions to final f and e states, such that parity conserving transitions display a more negative (or less positive) orientation than those for parity changing collisions. Closed shell QCT orientation moments are compared with QM $a_{1-}^{\{1\}}$ moments, which have been summed over initial and averaged final Λ -doublet level, in the middle panel of Figure 14. Both QCT and the summed and averaged QM moments show the same general trend, with $a_{1-}^{\{1\}}$ decreasing with increasing rotational excitation. The good agreement between these two sets of orientation moments suggests that the QM orientation can partly be accounted for in terms of the classical ‘attractive’ and ‘soft repulsive’ mechanisms discussed in Section ‘Rotational orientation in classical collisions’.

The Δj dependent oscillations that are evident in the Λ -doublet resolved QM data are

not seen for the QCT calculations. Such oscillations can be a result of parity dependent differences in the QM DCSs or due to the PDDCSs themselves. The origin of these oscillations can be explored by considering the “hybrid” orientation PP, displayed in the right hand panel of Figure 14. These hybrid orientation PP are constructed by integrating the product of the QCT renormalized PDDCSs, $[\rho_{1-}^{\{1\}}(\theta)]_{\text{QCT}}$, and the QM Λ -doublet resolved angular distribution, $[n_0^{\{0\}}(\theta)]_{\text{QM}}$, over $\cos \theta$, *i.e.*

$$[a_{1-}^{\{1\}}]_{\text{hybrid}} = \int d \cos \theta [n_{1-}^{\{1\}}]_{\text{hybrid}} = \int d \cos \theta [\rho_{1-}^{\{1\}}(\theta)]_{\text{QCT}} [n_0^{\{0\}}(\theta)]_{\text{QM}}. \quad (16)$$

While the hybrid PPs reproduce the decreasing trend in orientation with increasing Δj reasonably well, they fail to follow the oscillations seen in the $f-f$ QM orientation moments. The oscillations in the Λ -doublet resolved $a_{1-}^{\{1\}}$ moments must thus be a result of parity dependent differences in the polarization behavior itself. In a previous study of rotational alignment in the $\text{NO(X)} + \text{Ar}$ system, analogous “hybrid” *alignment* moments were able to reproduce very well the QM Λ -doublet resolved data.³ This reflects the underlying classical nature of rotational alignment, whereas the collision-induced rotational orientation is clearly significantly influenced by quantum mechanical effects, as discussed in Section ‘QM hard shell calculations’.

Conclusions

The rotational orientation after collisions of fully Λ -doublet state selected NO(X) with Ar has been investigated. Experimental normalized, $n_{1-}^{\{1\}}(\theta)$, and renormalized, $\rho_{1-}^{\{1\}}(\theta)$, polarization dependent differential cross-sections, and integral polarization parameters, $a_{1-}^{\{1\}}$, have been compared with CC QM calculations, and are found to be in very good agreement. In contrast, simulations performed using QCT calculations were unable to reproduce the orientation observed experimentally, or in the QM simulations.

The origins of the rotational orientation generated in the collisions of NO(X) and Ar at a

collisions energy of 530 cm^{-1} (66 meV) have also been investigated theoretically. Classical and quantum mechanical calculations have been used to demonstrate the effect of the attractive and soft repulsive parts of the potential on the rotational orientation, in comparison to collisions of hard shell species. For classical collisions, the symmetry of the collision of a hard shell results in no net rotational orientation. This symmetry is removed when a finite-range interaction potential is present.⁷ For collisions that take place on a soft repulsive potential, predominantly negative orientation is observed. In the presence of the full potential, clear features of the attractive region of the potential can be identified at low rotational excitation, leading to positive orientation. These two observations are in agreement with the limiting classical mechanisms proposed previously.^{5,7,11}

In contrast to the classical behavior, quantum mechanical encounters between hard shell molecules and atoms can also lead to collision-induced rotational orientation. This purely quantum mechanical effect arises because of the inherent non-local nature and finite duration time of the QM collision encounter.⁷ The QM mechanism for collision-induced rotational orientation is shown to play a significant role in the inelastic scattering of NO by Ar, particularly at high Δj , for which the collisions become more impulsive in nature.

Acknowledgement

The support of the UK EPSRC (to M.B. *via* Programme Grant EP/L005913/1), the EU (to M.B. *via* FP7 EU People ITN project 238671), and the Spanish Ministry of Science and Innovation (grants CTQ2012-37404 and CSD2009-00038, to FJA) are gratefully acknowledged. S.S. acknowledges support from the National Basic Research Program of China (973 program) under grant No. 2013CB922200, and from the National Science Foundation of China under grant Nos. 11034003 and 91221301. SDSG and MB also thank Cambio Ltd. and Dr Peter Dean for generous support.

References

- (1) Kim, S. K.; Herschbach, D. R. Angular Momentum Disposal in Atom Exchange Reactions. *Faraday Discuss. Chem. Soc.* **1987**, *84*, 159.
- (2) Cline, J. I.; Lorenz, K. T.; Wade, E. A.; Barr, J. W.; Chandler, D. W. Ion imaging measurement of collision-induced rotational alignment in Ar-NO scattering. *J. Chem. Phys.* **2001**, *115*, 6277.
- (3) Brouard, M.; Chadwick, H.; Eyles, C. J.; Hornung, B.; Nichols, B.; Aoiz, F. J.; Jambolina, P. G.; Stolte, S.; de Miranda, M. P. Rotational alignment effects in NO(X) + Ar inelastic collisions: A theoretical study. *J. Chem. Phys.* **2013**, *138*.
- (4) Brouard, M.; Chadwick, H.; Eyles, C. J.; Hornung, B.; Nichols, B.; Aoiz, F. J.; Jambolina, P. G.; Stolte, S. Rotational alignment effects in NO(X) + Ar inelastic collisions: An experimental study. *J. Chem. Phys.* **2013**, *138*.
- (5) Alexander, M. H. Close-coupling studies of orientation dependence of rotationally inelastic collisions. *J. Chem. Phys.* **1977**, *67*, 2703.
- (6) Lorenz, K. T.; Chandler, D. W.; Barr, J. W.; Chen, W.; Barnes, G. L.; Cline, J. I. Direct measurement of the preferred sense of NO rotation after collision with argon. *Science* **2001**, *293*, 2063.
- (7) Brouard, M.; Hornung, B.; Aoiz, F. J. Origin of collision-induced molecular orientation. *Phys. Rev. Lett.* **2013**, *111*, 183202.
- (8) Aoiz, F. J.; Herrero, V. J.; Rábanos, V. S.; Verdasco, J. E. Classical stereodynamics in Ar plus NO inelastic collisions. *Phys. Chem. Chem. Phys.* **2004**, *6*, 4407.
- (9) Jambolina, P. G.; Kłos, J.; Aoiz, F. J.; de Miranda, M. P. New findings regarding the NO angular momentum orientation in Ar-NO($^2\Pi_{1/2}$) collisions. *Phys. Chem. Chem. Phys.* **2012**, *14*, 9826.

- (10) Aoiz, F. J.; Brouard, M.; Enriquez, P. A. Product rotational polarization in photon-initiated bimolecular reactions. *J. Chem. Phys.* **1996**, *105*, 4964.
- (11) Aoiz, F. J.; Brouard, M.; Herrero, V. J.; Rabanos, V. S.; Stark, K. Product rotational polarization. The stereodynamics of the $F + H_2$ reaction. *Chem. Phys. Lett.* **1997**, *264*, 487–494.
- (12) de Miranda, M. P.; Aoiz, F. J.; Bañares, L.; Rábanos, V. S. A unified quantal and classical description of the stereodynamics of elementary chemical reactions: State-resolved $\mathbf{k-k'-j'}$ vector correlation for the $H + D_2(v = 0, j = 0)$ reaction. *J. Chem. Phys.* **1999**, *111*, 5368.
- (13) Aldegunde, J.; Aoiz, F. J.; González-Sánchez, L.; Jambrina, P. G.; de Miranda, M. P.; Sáez-Rábanos, V. Orientation effects in $Cl + H_2$ inelastic collisions: characterization of the mechanisms. *Phys. Chem. Chem. Phys.* **2012**, *14*, 2911–2920.
- (14) Rakitzis, T. P.; Kandel, S. A.; Lev-On, T.; Zare, R. N. Differential cross section polarization moments: Location of the D-atom transfer in the transition-state region for the reactions $Cl + C_2D_6 \rightarrow DCl(v' = 0, j' = 1) + C_2D_5$ and $Cl + CD_4 \rightarrow DCl(v' = 0, j' = 1) + CD_3$. *J. Chem. Phys.* **1997**, *107*, 9392–9405.
- (15) Chadwick, H.; Nichols, B.; Gordon, S. D. S.; Hornung, B.; Squires, E.; Brouard, M.; Klos, J.; Alexander, M. H.; Aoiz, F. J.; Stolte, S. Inelastic Scattering of NO by Kr: Rotational Polarization over a Rainbow. *J Phys. Chem. Lett.* **2014**, *5*, 3296–3301.
- (16) Alexander, M. H. Rotationally inelastic collisions between a diatomic molecule in a $^2\Pi$ electronic state and a structureless target. *J. Chem. Phys.* **1982**, *76*, 5974.
- (17) Alexander, M. H. Quantum treatment of rotationally inelastic collisions involving molecules in Π -electronic states - new derivation of the coupling potential. *Chem. Phys.* **1985**, *92*, 337.

- (18) Alexander, M. H. Differential and integral cross-sections for the inelastic scattering of NO($X^2\Pi$) by Ar on a new *ab initio* potential energy surface. *J. Chem. Phys.* **1993**, *99*, 7725.
- (19) Alexander, M. H. A new, fully *ab initio* investigation of the NO($X^2\Pi$)Ar system. I. Potential energy surfaces and inelastic scattering. *J. Chem. Phys.* **1999**, *111*, 7426.
- (20) Suits, A. G.; Bontuyan, L. S.; Houston, P. L.; Whitaker, B. J. Differential cross-sections for the state-selected products by direct imaging - Ar + NO. *J. Chem. Phys.* **1992**, *96*, 8618.
- (21) Jons, S. D.; Shirley, J. E.; Vonk, M. T.; Giese, C. F.; Gentry, W. R. State-to-state differential cross-sections for rotationally inelastic multiplet-conserving and multiplet-changing collisions of NO ($^2\Pi_{1/2}, j = 0.5$) with Ar. *J. Chem. Phys.* **1992**, *97*, 7831.
- (22) Jons, S. D.; Shirley, J. E.; Vonk, M. T.; Giese, C. F.; Gentry, W. R. State-to-state differential cross sections for rotationally inelastic collisions of NO($^2\Pi_{1/2}, j = 0.5$) with Ar at kinetic energies between 117 cm^{-1} and 1694 cm^{-1} . *J. Chem. Phys.* **1996**, *105*, 5397.
- (23) Bontuyan, L. S.; Suits, A. G.; Houston, P. L.; Whitaker, B. J. State-resolved differential cross-sections for the crossed-beam Ar-NO inelastic-scattering by direct ion imaging. *J. Phys. Chem.* **1993**, *97*, 6342.
- (24) Elioff, M. S.; Chandler, D. W. State-to-state differential cross sections for spin-multiplet-changing collisions of NO($X^2\Pi_{1/2}$) with argon. *J. Chem. Phys.* **2002**, *117*, 6455.
- (25) Aoiz, F. J.; Verdasco, J. E.; Herrero, V. J.; Rábanos, V. S.; Alexander, M. H. Attractive and repulsive interactions in the inelastic scattering of NO by Ar: A comparison between classical trajectory and close-coupling quantum mechanical results. *J. Chem. Phys.* **2003**, *119*, 5860.

- (26) Eyles, C. J.; Brouard, M.; Yang, C.-H.; Kłos, J.; Aoiz, F. J.; Gijsbertsen, A.; Wiskerke, A. E.; Stolte, S. Interference structures in the differential cross-sections for inelastic scattering of NO by Ar. *Nature Chemistry* **2011**, *3*, 597.
- (27) Eyles, C. J.; Brouard, M.; Chadwick, H.; Hornung, B.; Nichols, B.; Yang, C.-H.; Kłos, J.; Aoiz, F. J.; Gijsbertsen, A.; Wiskerke, A. E. et al. Fully lambda-doublet resolved state-to-state differential cross-sections for the inelastic scattering of NO(X) with Ar. *Phys. Chem. Chem. Phys.* **2012**, *14*, 5403.
- (28) Eyles, C. J.; Brouard, M.; Chadwick, H.; Aoiz, F. J.; Kłos, J.; Gijsbertsen, A.; Zhang, X.; Stolte, S. The effect of parity conservation on the spin-orbit conserving and spin-orbit changing differential cross sections for the inelastic scattering of NO(X) by Ar. *Phys. Chem. Chem. Phys.* **2012**, *14*, 5420.
- (29) von Zastrow, A.; Onvlee, J.; Vogels, S. N.; Groenenboom, G. C.; van der Avoird, A.; van de Meerakker, S. Y. T. State-resolved diffraction oscillations imaged for inelastic collisions of NO radicals with He, Ne and Ar. *Nature Chemistry* **2014**, *6*, 216–221.
- (30) Vogels, S. N.; Onvlee, J.; von Zastrow, A.; Groenenboom, G. C.; van der Avoird, A.; van de Meerakker, S. Y. T. High-Resolution Imaging of Velocity-Controlled Molecular Collisions Using Counterpropagating Beams. *Phys. Rev. Lett.* **2014**, *113*, 263202.
- (31) Onvlee, J.; Vogels, S. N.; van der Avoird, A. D.; Groenenboom, G. C.; van de Meerakker, S. Y. T. Resolving rainbows with superimposed diffraction oscillations in NO plus rare gas scattering: experiment and theory. *New J. Phys.* **2015**, *17*.
- (32) Wade, E. A.; Lorenz, K. T.; Chandler, D. W.; Barr, J. W.; Barnes, G. L.; Cline, J. I. Ion imaging studies of product rotational alignment in collisions of NO ($X^2\Pi_{1/2}$, $j = 0.5$) with Ar. *Chem. Phys.* **2004**, *301*, 261.
- (33) Gijsbertsen, A.; Linnartz, H.; Rus, G.; Wiskerke, A. E.; Stolte, S.; Chandler, D. W.;

- Kłos, J. Differential cross sections for collisions of hexapole state-selected NO with He. *J. Chem. Phys.* **2005**, *123*, 224305.
- (34) Eppink, A. T. J. B.; Parker, D. H. Velocity map imaging of ions and electrons using electrostatic lenses: Application in photoelectron and photofragment ion imaging of molecular oxygen. *Rev. Sci. Instrum.* **1997**, *68*, 3477.
- (35) Chandler, D. W.; Houston, P. L. Two-dimensional imaging of state-selected photodissociation products detected by multiphoton ionization. *J. Chem. Phys.* **1987**, *87*, 1445.
- (36) Alexander, A. J. Determination of the helicity of oriented photofragments. *Chem. Phys.* **2005**, *132*, 194312.
- (37) Brouard, M.; Chadwick, H.; Gordon, S. D. S.; Hornung, B.; Nichols, B.; Kłos, J.; Aoiz, F. J.; Stolte, S. Fully quantum state-resolved inelastic scattering of NO (X)+ Kr: Differential cross sections and product rotational alignment. *J. Chem. Phys.* **2014**, *141*, 164306.
- (38) Aldegunde, J.; de Miranda, M. P.; Haigh, J. M.; Kendrick, B. K.; Sáez-Rábanos, V.; Aoiz, F. J. How reactants polarization can be used to change and unravel chemical reactivity. *J. Phys. Chem. A* **2005**, *109*, 6200–6217.
- (39) Hertel, I. V.; Stoll, W. Collision experiments with laser excited atoms in crossed beams. *Adv. At. Mol. Phys.* **1978**, *13*, 113.
- (40) Alexander, M. H. Propensity rules for rotationally inelastic collisions of symmetric top molecules or linear polyatomic molecules with structureless atoms. *J. Chem. Phys.* **1982**, *77*, 1855.
- (41) Brouard, M.; Chadwick, H.; Eyles, C. J.; Hornung, B.; Nichols, B.; Scott, J. M.; Aoiz, F. J.; Kłos, J.; Stolte, S.; Zhang, X. The fully quantum state-resolved inelastic scattering of NO(X) + Ne: experiment and theory. *Mol. Phys.* **2013**, *111*, 1759.

- (42) Beck, D.; Ross, U. Rotationally inelastic, classical scattering from an anisotropic rigid shell potential of rotation symmetry. *Z. Phys.* **1979**, *293*, 107.
- (43) Buck, U.; Huisken, F.; Pauly, H.; Schleusener, J. Intermolecular potentials by the inversion of differential cross sections. V. ArKr. *J. Chem. Phys.* **1978**, *68*, 3334.
- (44) Kreutz, T. G.; Flynn, G. W. Analysis of translationa;, rotational, and vibrational-energy transfer in collision between CO₂ and hot hydrogen-atoms - The 3-dimensional breathing ellipsoid model. *J. Chem. Phys.* **1990**, *93*, 452.
- (45) Bosanac, S. 2-dimensional model of rotationally inelastic collisions. *Phys. Rev. A* **1980**, *22*, 2617.
- (46) Aoiz, F. J.; Herreo, V. J.; Rabanos, V. S. Quasiclassical state to state reaction cross sections for D+H₂($v = 0, j = 0$) \rightarrow HD(v, j) + H. Formation and characteristics of short-lived collision complexes. *J. Chem. Phys.* **1992**, *97*, 7423.
- (47) Bosanac, S. D.; Petrovic, N. Quantum theory of impulsive collisions. *Phys. Rev. A* **1990**, *41*, 5909.
- (48) Bosanac, S. D.; Murrell, J. N. Hard Shell potentials from rotational state-to-state inelastic scattering - a possible route to inversion. *J. Chem. Phys.* **1991**, *94*, 1167.
- (49) HIBRIDON is a package of programs for the time-independent quantum treatment of inelastic collisions and photodissociation written by M. H. Alexander, D. E. Manolopoulos, H.-J. Werner, and B. Follmeg, with contributions by P. F. Vohralik, D. Lemoine, G. Corey, R. Gordon, B. Johnson, T. Orlikowski, A. Berning, A. Degli-Esposti, C. Rist, P. Dagdigian, B. Pouilly, G. van der Sanden, M. Yang, F. de Weerd, S. Gregurick, and J. Kłos.

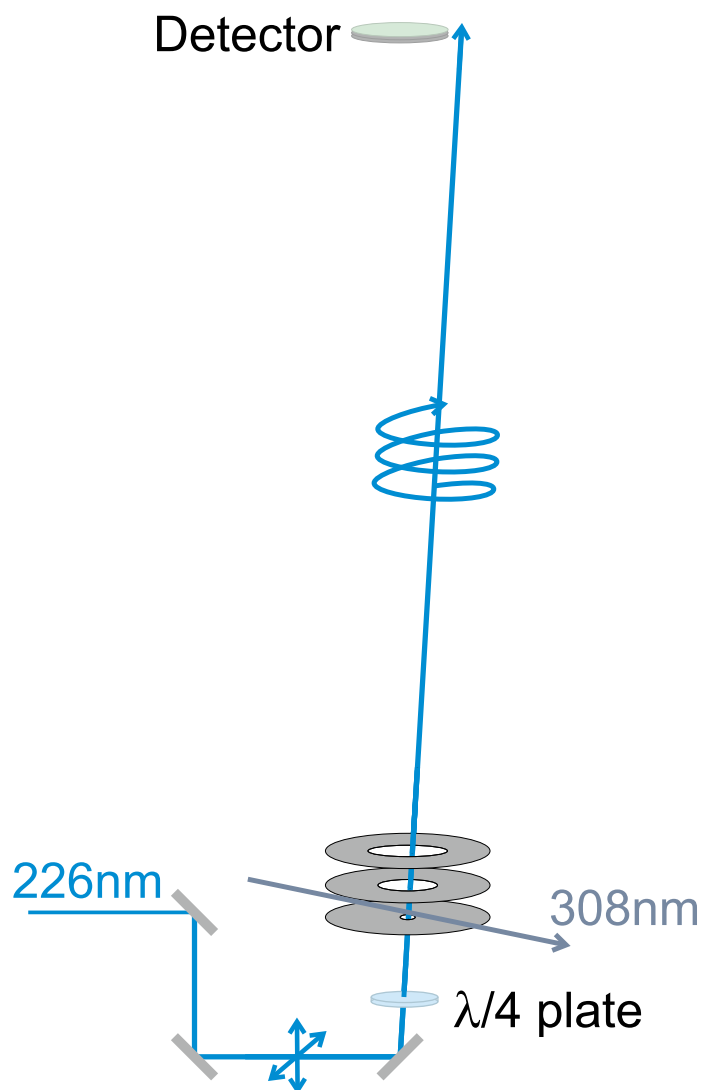


Figure 1: Schematic of the experimental setup of the interaction volume. The excitation laser is directed perpendicular to the plane defined by the molecular beams and towards the detector.⁶ To avoid hitting the detector, the laser was directed off-axis by approximately 2 degrees. The circularly polarized light is generated using a photo-elastic modulator and quarter wave plate.

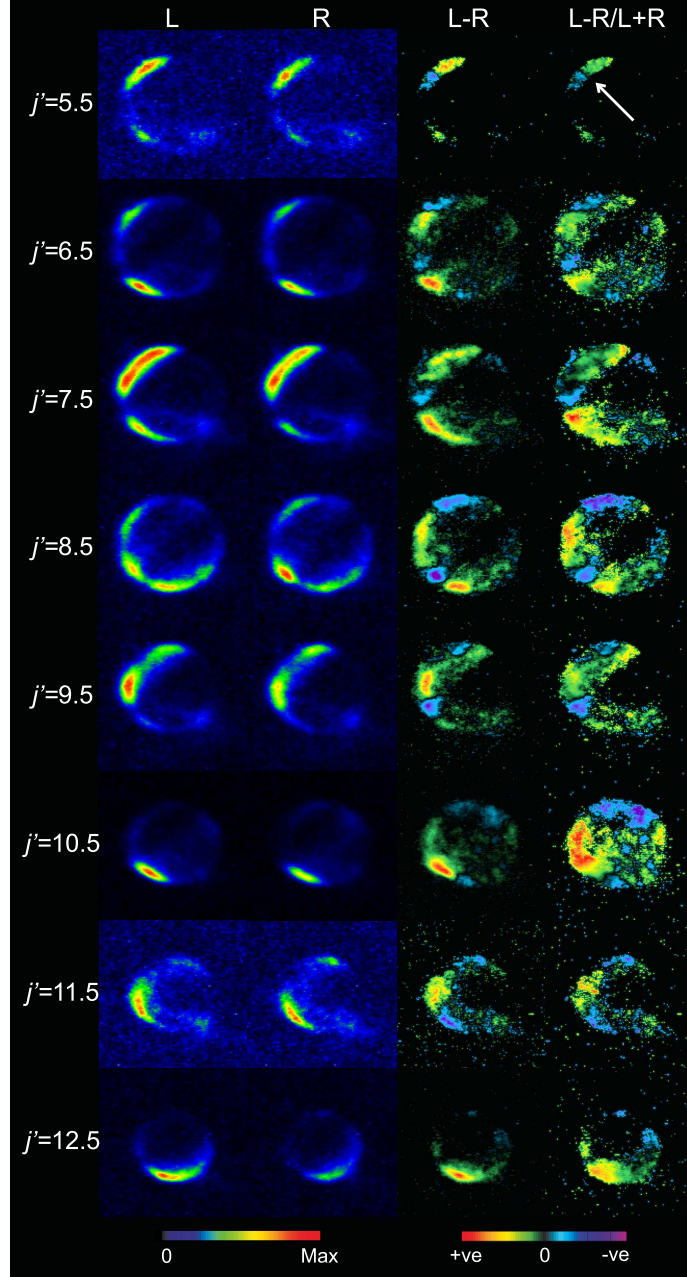


Figure 2: Experimental difference ($I_L - I_R$), normalized difference $(I_L - I_R)/(I_L + I_R)$ and individual I_L and I_R DCS images for transitions between $|\Omega = 0.5, j = 0.5, f\rangle \rightarrow |\Omega' = 0.5, j', f\rangle$ where $j' = 5.5$ to 12.5 . The direction of the relative velocity is shown by a white arrow in the top right image.

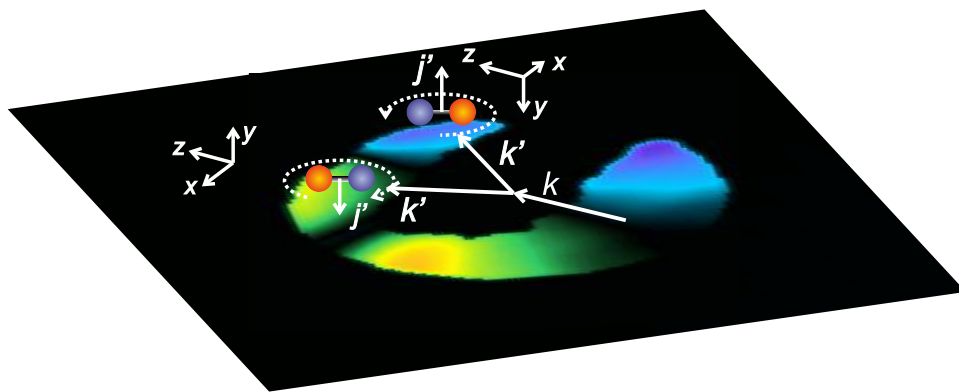


Figure 3: Illustration of the rotational orientation after a collision of NO(X) with Ar resulting for the $j' = 12.5, f$ state. The x, y and z axes of the scattering frame are shown for each side of the image.

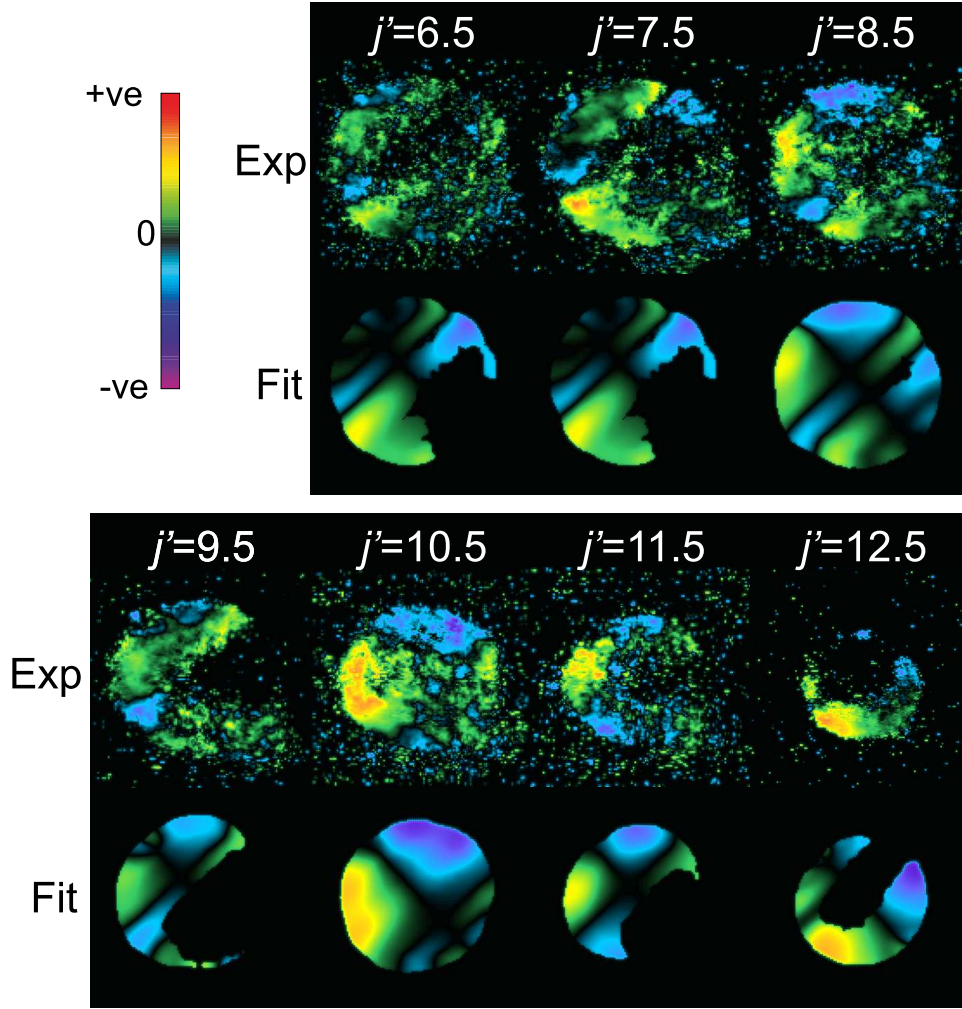


Figure 4: Experimental (top row) and fitted (bottom row) normalized difference ion images $(I_L - I_R)/(I_L + I_R)$ for spin-orbit conserving $f - f$ transitions.

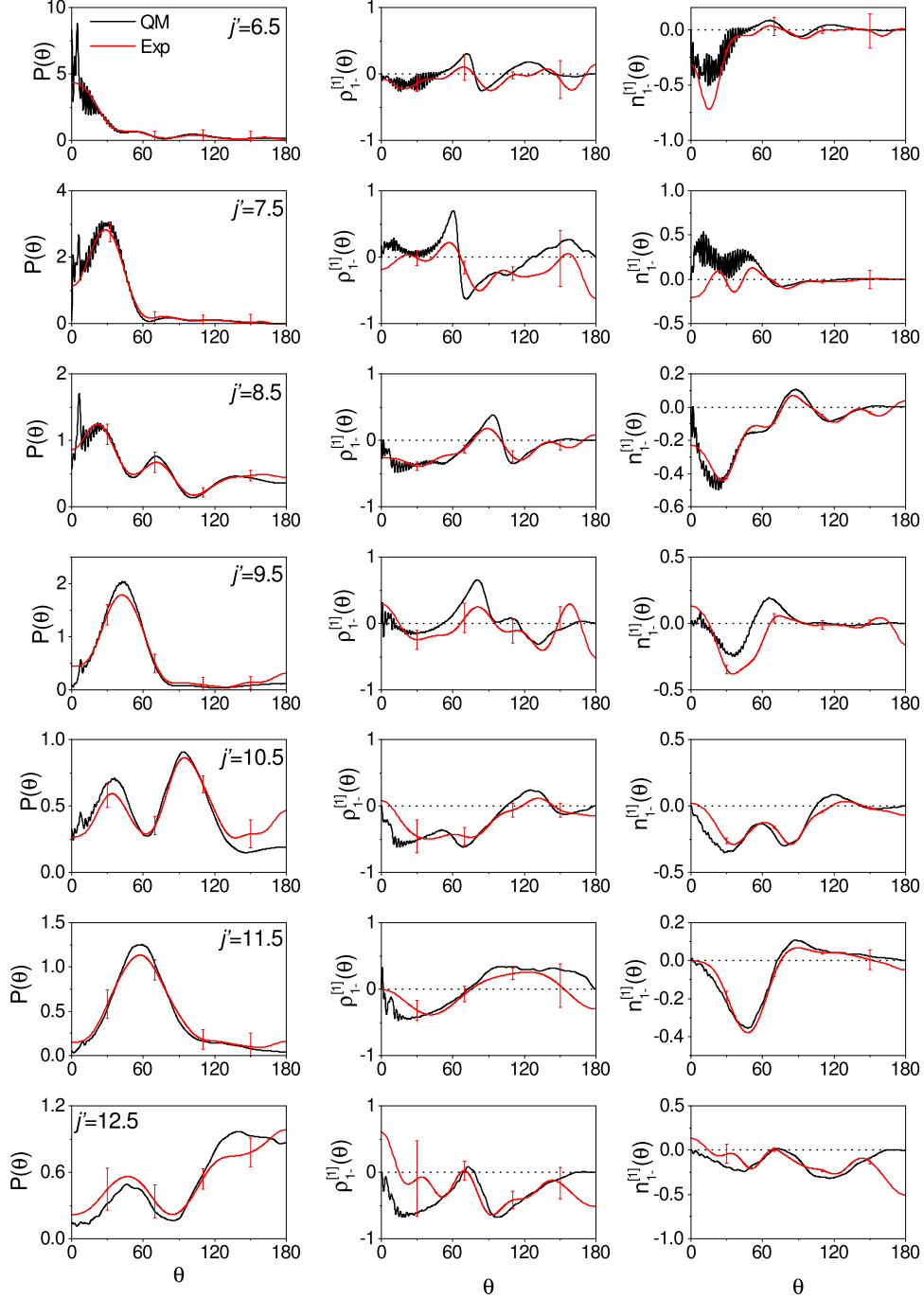


Figure 5: Experimentally determined (red line) and QM calculated (black line) normalized angular distributions (left column), renormalized $\rho_{1-}^{\{1\}}(\theta)$ PDDCSs (centre column) and normalized $n_{1-}^{\{1\}}(\theta)$ PDDCSs (right column). The data are for spin-orbit conserving $f - f$ transitions. The error bars on the experimental data represent the 95 % confidence limits.

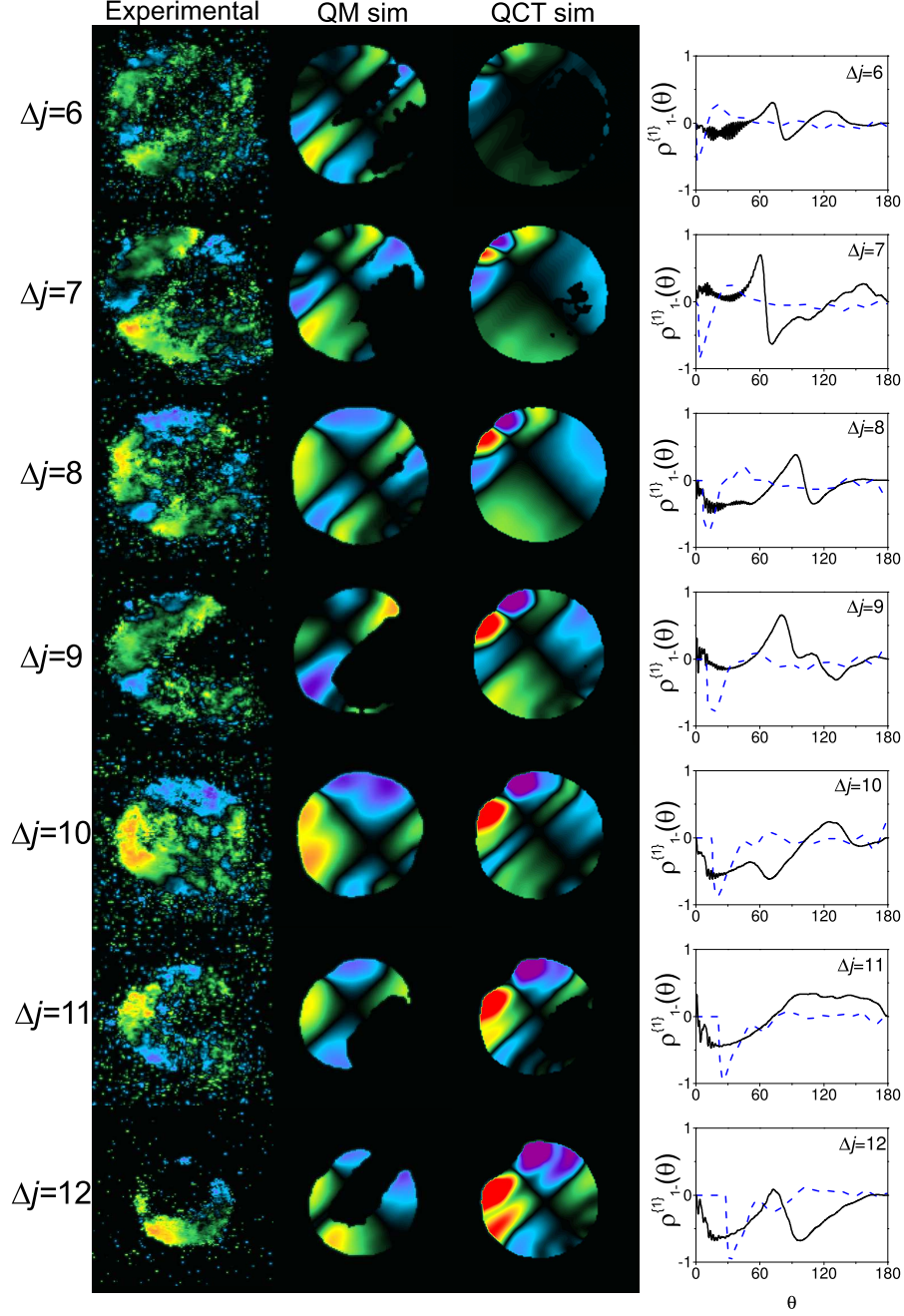


Figure 6: Experimental, open shell QM simulated and closed shell QCT simulated normalized difference $(I_L - I_R)/(I_L + I_R)$ images for transitions between $\Delta j = 6 - 12$. The experimental images and QM simulations are for spin-orbit conserving $f - f$ states. The corresponding QM and QCT $\rho_{1-}^{\{1\}}(\theta)$ moments from open shell QM (black solid line) and closed shell QCT calculations (blue dashed line) are shown in the fourth column.

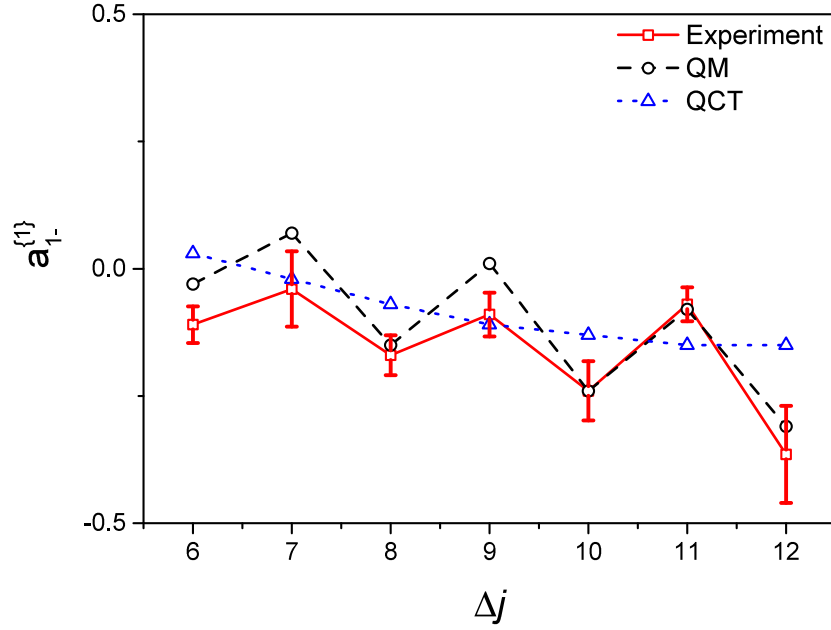


Figure 7: Comparison of experimentally determined (red squares) integral polarization parameters, $a_{1-}^{\{1\}}$, with their QM and QCT counterparts for $\Delta j=6-12$ transitions. The QM data are for spin-orbit conserving $f-f$ transitions, while the QCT calculations are inherently closed shell. For the transitions shown $\Delta j = \text{even}$ are parity conserving, while $\Delta j = \text{odd}$ are parity changing. The error bars on the experimental data represent the 95 % confidence limits. Note that the classical limits of the orientation PP are $-1 \leq a_{1-}^{\{1\}} \leq +1$.

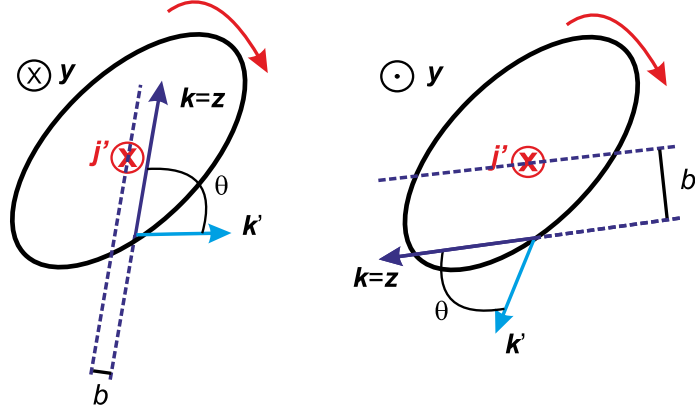


Figure 8: Two classical trajectories leading to scattering for the same Δj and scattering angle, θ , but leading to equal and opposite rotational angular momentum orientation. The trajectory on the left induces rotational polarization along $-y$, while that on the right induces polarization along $+y$, with the net effect that there is no orientation in the classical hard shell model.

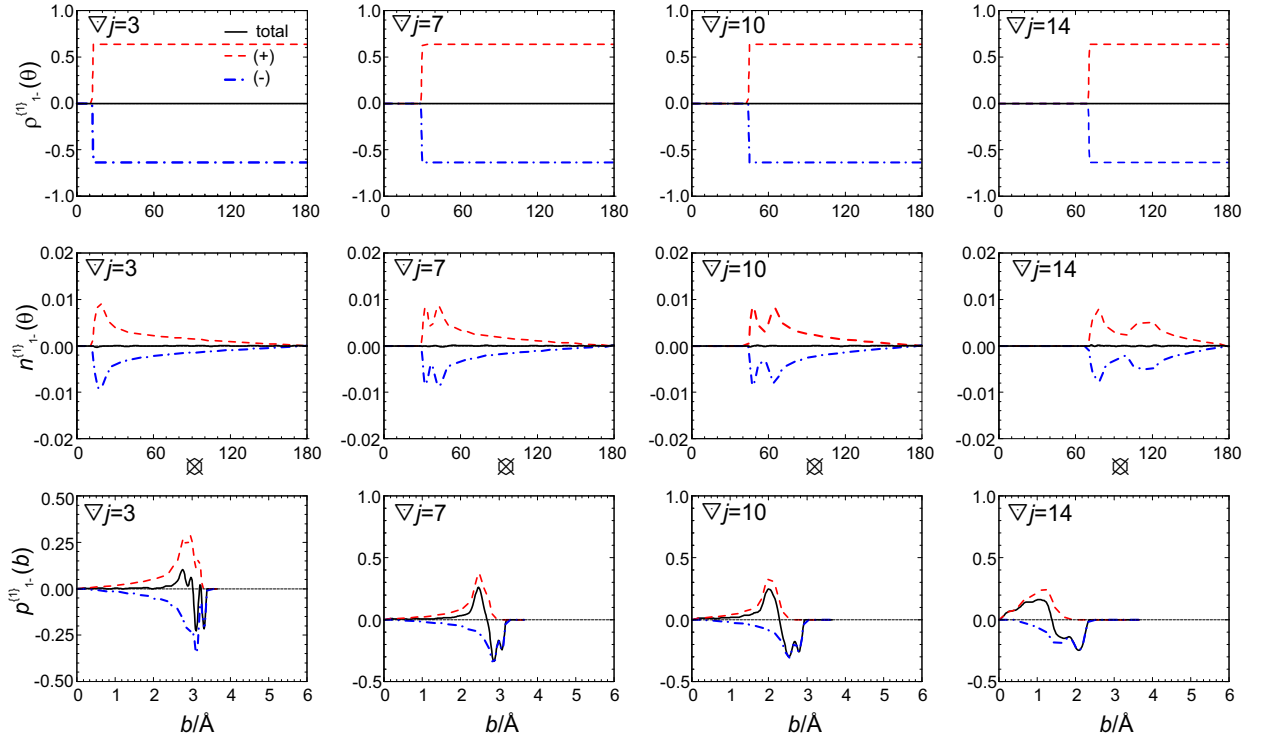


Figure 9: Top row: Classical hard shell total (black solid line) and orientation resolved renormalized PDDCSs ($(+)$ red dashed line, $(-)$ blue dash-dotted line), $\rho_{1-}^{\{1\}}(\theta)$. Middle row: The total and normalized PDDCSs, $n_{1-}^{\{1\}}(\theta)$. Bottom row: Orientation resolved n-PDDCSs, $p_{1-}^{\{1\}}(b)$ (see text for its definition). The different columns corresponds to the $\Delta j = 3, 7, 10$ and 14 transitions from left to right.

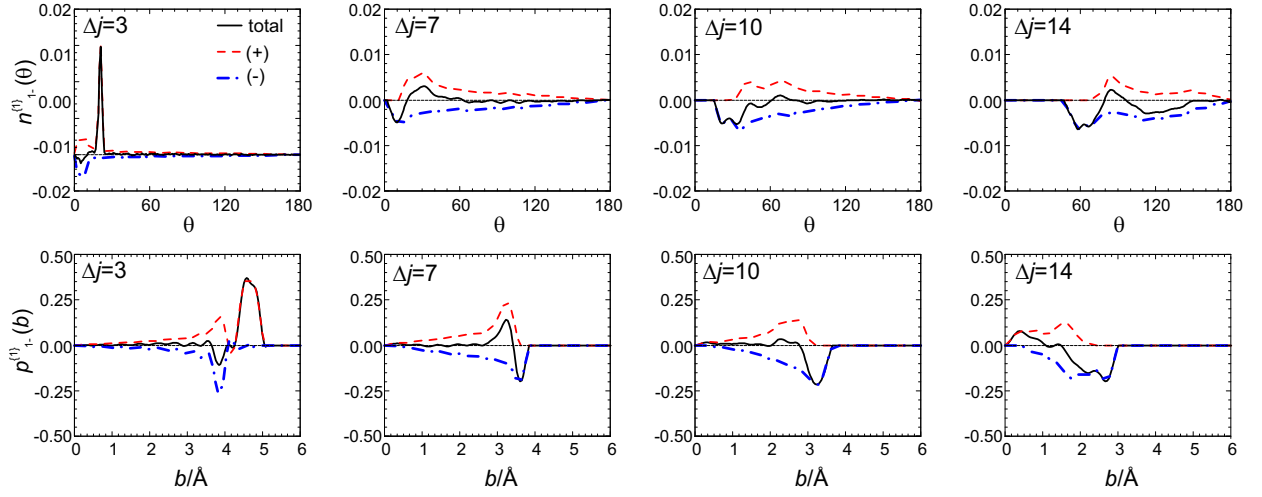


Figure 10: The QCT total (black solid line) and orientation resolved normalized PDDCSs ((+) red dashed line, (-) blue dash-dotted line), $n_{1-}^{\{1\}}(\theta)$ employing the full $V_{\text{sum}}(R, \gamma)$ potential are shown in the top row for the $\Delta j = 3, 7, 10$ and 14 transitions from left to right. The corresponding total and orientation resolved n-PDPCSs, $p_{1-}^{\{1\}}(b)$, are shown in the bottom row.

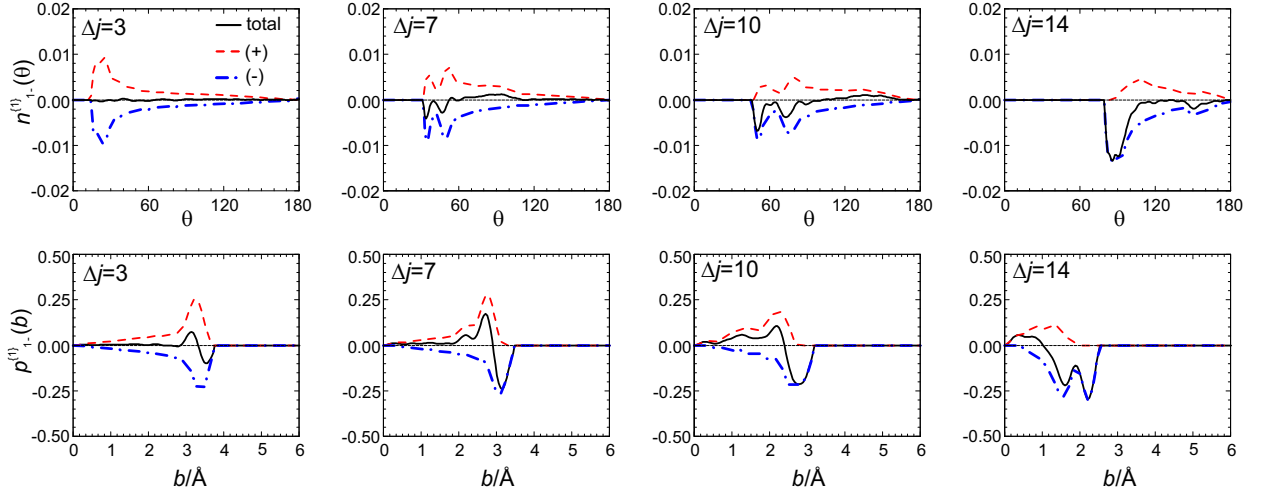


Figure 11: The QCT total (black solid line) and orientation resolved normalized PDDCSs ((+) red dashed line, (-) blue dash-dotted line), $n_{1-}^{\{1\}}(\theta)$ employing the purely repulsive $V_{\text{sum}}(R, \gamma)$ potential are shown in the top row for the $\Delta j = 3, 7, 10$ and 14 transitions from left to right. The corresponding total and orientation resolved n-PDPCSs, $p_{1-}^{\{1\}}(b)$, are shown in the bottom row.

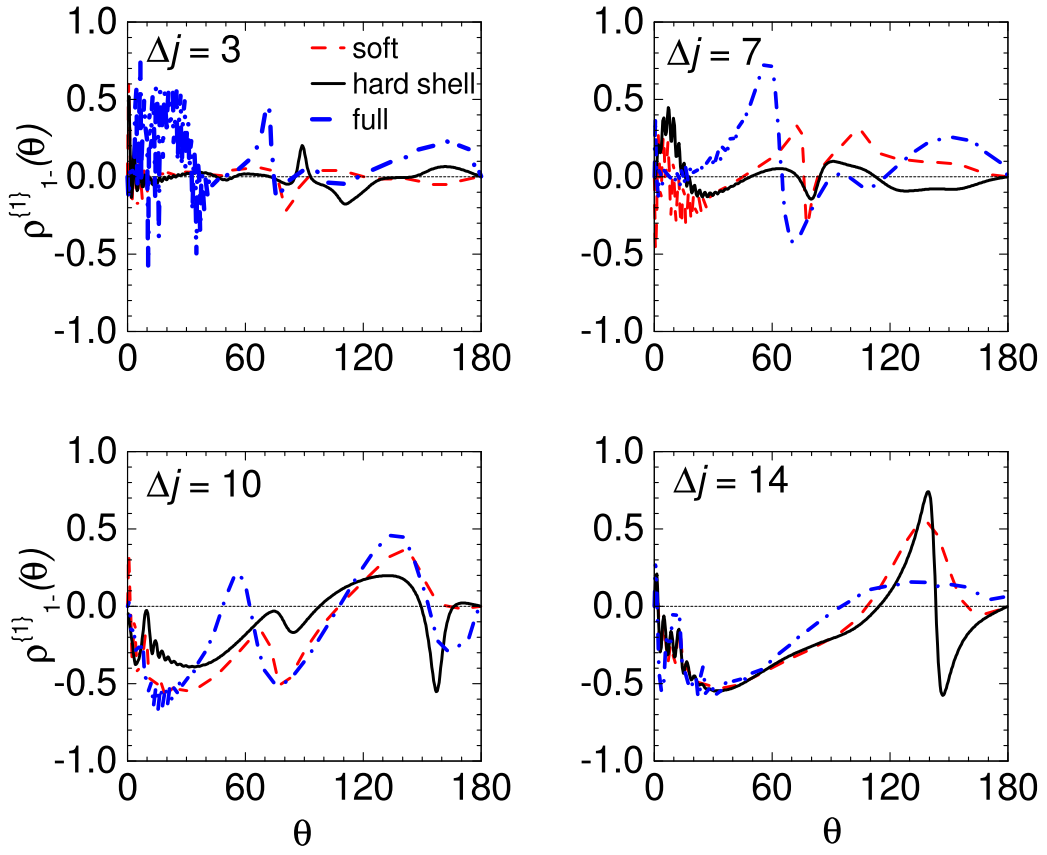


Figure 12: Hard-shell QM (black solid line), soft potential CC QM (red dashed line) and full potential (blue dash-dotted line) renormalized PDDCSs, $\rho_{1-}^{(1)}(\theta)$, for the indicated Δj transitions.

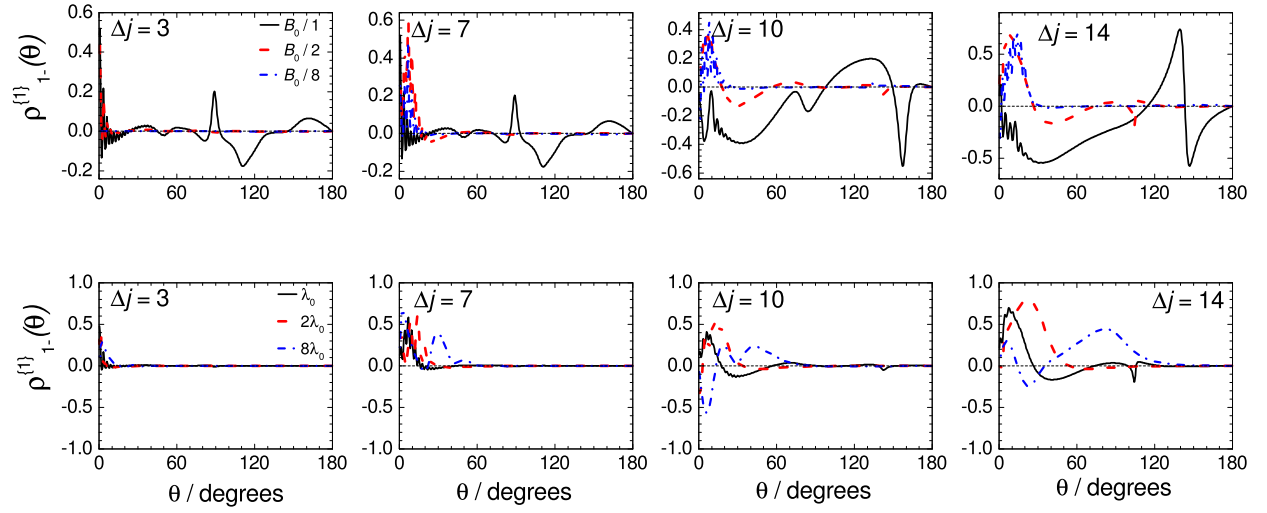


Figure 13: Closed shell hard-shell QM calculations of the renormalized PDDCS, $\rho_{1-}^{\{1\}}(\theta)$, for the $\Delta j = 3, 7, 10, 14$ transitions, showing the dependence of the orientation on the rotational constant (top row) and on the de Broglie wavelength (bottom row). Top row: unscaled, B_0 (black solid line), $B_0/2$ (red dashed line line) and $B_0/8$ (blue dash-dotted line). Bottom row: de Broglie wavelength unscaled, λ_0 (black solid line), $2\lambda_0$ (red dashed line line) and $8\lambda_0$ (blue dash-dotted line). For the calculations presented in the bottom row, the rotational constant was set to $B_0/2$.

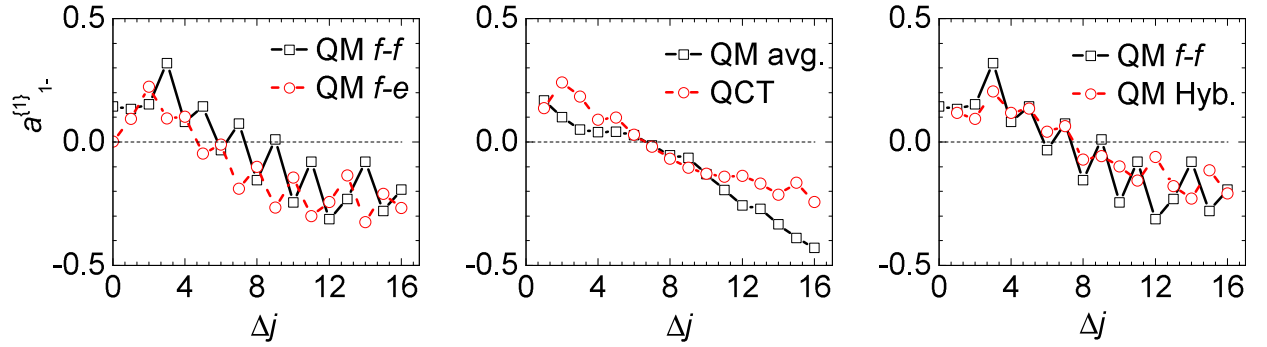


Figure 14: Left panel: The CC QM orientation moments for the $|j, 0.5, -1\rangle \rightarrow |j', 0.5, -1\rangle$ ($f-f$) transitions (black open squares) and for the $|j, 0.5, -1\rangle \rightarrow |j', 0.5, +1\rangle$ ($f-e$) transitions (red open circles). Middle panel: Comparison of the CC QM orientation moments summed over the final and averaged over the initial Λ -doublet levels (black open squares) and QCT orientation moments (red open circles). Right panel: The CC QM (black open squares) and hybrid (red open circles) orientation moments for the $|j, 0.5, -1\rangle \rightarrow |j', 0.5, -1\rangle$ transitions. Note that the classical limits of the orientation PP are $-1 \leq a_{1-}^{\{1\}} \leq +1$.

Graphical TOC Entry

